Materials Today Advances 9 (2021) 100132

Contents lists available at ScienceDirect

Materials Today Advances

journal homepage: www.journals.elsevier.com/materials-today-advances/

Spectral neutron tomography

K.V. Tran [a, b, c, **], R. Woracek [d, *], N. Kardjilov [a], H. Markötter [a, h], A. Hilger [a], W. Kockelmann [e], J. Kelleher [e], S.B. Puplampu [f], D. Penumadu [f], A.S. Tremsin [g], J. Banhart [a, b], I. Manke [a]

[a] Helmholtz-Zentrum Berlin für Materialien und Energie GmbH, Hahn-Meitner-Platz 1, 14109, Berlin, Germany
[b] Technische Universität Berlin, Straße des 17. Juni 135, 10623, Berlin, Germany
[c] Thuyloi University, 175 Tay Son, Dong Da, Hanoi, Viet Nam
[d] European Spallation Source ESS ERIC, SE-221 00, Lund, Sweden
[e] STFC-Rutherford Appleton Laboratory, ISIS Facility, Harwell, OX11 0QX, UK
[f] The University of Tennessee Knoxville, TN, 37996-2313, USA
[g] University of California at Berkeley, Berkeley, CA, 94720, USA
[h] Bundesanstalt für Materialforschung und -Prüfung, Unter Den Eichen 87, 12205, Berlin, Germany

ARTICLE INFO

Article history:
Received 7 November 2020
Received in revised form
20 December 2020
Accepted 21 December 2020
Available online xxx

Keywords:
4D tomographic data
Multi-energy CT
Spectral CT
Phase distribution
Bulk sample
Full-field phase tomography

ABSTRACT

Combined three-dimensional (3D) mapping of (micro-)structures with elemental and crystalline phase variations is of significant importance for the characterization of materials. Neutron wavelength selective imaging is a spectral imaging technique that exploits unique contrast differences e.g. for mapping dissimilar elemental, isotope, or phase compositions, and has the particular advantage of being applicable to sample volumes on the meso- and macroscale. While being mostly applied as radiography (2D) so far, we herein report that the extension to tomography allows for the display of the full spectral information for every voxel and in 3D. The development is supported by example data from a continuous as well as a pulsed neutron source. As a practical example, we collected 4D data sets (3D + spectral) of plastically deformed metastable stainless steel and herein demonstrate an improved quantification strategy for crystalline phase fractions. These exemplary results illustrate that localized phase transformations can be quantified even in complex geometries within centimeter-sized samples, and we will discuss the limits and future prospects of the technique that is not limited to crystalline materials.

1. Introduction

Dual/multi-energy and spectral transmission imaging methods exploit the dependence of a material's attenuation characteristics on the energy of the penetrating radiation and hence allow to differentiate between materials of different elemental compositions. Such methods have been successful not only in medical X-ray imaging to discriminate e.g. different types of tissue in the presence of contrast agents [1], but also in materials science and biology, using both X-rays [2–8] as well as electrons [9,10]. While dual energy imaging was possible for a long time using X-rays of different energies [11,12], a redefining development for spectral CT was the advent of energy sensitive area detectors that allow using a polychromatic beam. Similarly, multi-energy neutron imaging [13–17] became feasible with the availability of double-crystal monochromators at steady-state sources [18,19] but can be used much more efficiently by the time-of-flight (TOF) technique at spallation sources [20–22]. While a well-defined monochromatized beam is a pre-requisite for several neutron imaging modalities [23–25], the neutron-energy-dependent attenuation characteristics of samples often provide invaluable information by themselves.

In this article, we introduce quantitative spectral neutron tomography, which is based on four-dimensional data sets (3D volume information plus the energy dependence of a material's linear attenuation coefficient). As a practical example, we demonstrate crystalline phase tomography by enabling the display and evaluation of energy-dependent attenuation coefficients on a voxel-by-voxel basis. The fact that materials with different composition

* Corresponding author.
** Corresponding author.
E-mail addresses: khanhtv@tlu.edu.vn (K.V. Tran), robin.woracek@ess.eu (R. Woracek).

https://doi.org/10.1016/j.mtadv.2021.100132

and structures possess energy-dependent neutron attenuation characteristics [26,27] is being exploited in absorption contrast transmission imaging by the instrument design, while it is more explicitly evaluated e.g. by diffraction contrast [28], resonance absorption contrast [29,30], or inelastic scattering contrast [31]. Most published work based on neutron energy dependencies in transmission imaging has focused on radiographic projections so far, with notable exceptions including crystalline phase tomography [32–35] and special cases of strain tomography [36–39] that both exploit diffraction contrast and temperature and isotope-specific tomography based on resonance absorption contrast [22,40,41].

Fig. 1 shows the energy dependence of the attenuation characteristics for some selected materials for both X-rays and neutrons. For X-rays, the well-known approach to exploit X-ray absorption edges is highlighted by comparing cathode materials in different lithium intercalation states as found during operation of batteries. By analogy, energy-dependent attenuation characteristics exist also for neutrons e.g. yielding information about microstructures and phase compositions, as abrupt changes can be observed at Bragg edges that are characteristic to the crystalline structures. Energy dependencies for both radiation types enable applications in various areas. For the remainder of the article, we will refer to wavelength rather than energy when describing the method as this is more commonly used for neutron imaging.

As exemplified by Fig. 1, one can expect that spectral neutron tomography will be beneficial for a wide array of materials and applications. To demonstrate its potential, we herein apply it to the tomographic reconstruction of phase fractions within samples made from metastable stainless steel that exhibit the transformation-induced plasticity (TRIP) effect under plastic deformation. This example exploits the diffraction contrast based on differences of the crystalline structure within the sample and was selected because it is well understood and supported by reference data. It should be noted, however, that the main challenge in exploiting diffraction contrast in transmission imaging lies in the fact that many crystalline properties have a pronounced directional dependence (i.e. are tensorial). This renders tomographic reconstructions challenging not only for neutrons but also for electrons [9] or X-rays [2]. For tomographic investigations of single or oligo-crystals, one can create suitable boundary conditions [42,43] and perform diffractive imaging by analyzing diffraction spots from individual grains [44,45]. In the case of polycrystalline samples, which represent the majority of metallic alloys, the number and sizes of grains do typically not allow one to analyze individual diffraction spots. In such cases and for materials with suitable coherent scattering cross section and a high symmetry, one can use the Bragg edges in transmission spectra to study localized strain, phase, and texture differences [28]. If the grains are randomly distributed, non-tensorial properties such as crystalline phase fractions can be reconstructed from transmission images alone [32,33,35,46,47]. For samples with preferred grain orientations (texture), however, the widely used filtered back projection algorithm is not applicable, even for the reconstruction of non-tensorial properties. This challenge may only be circumvented with suitable models to aid the quantitative interpretation of neutron transmission data for textured samples and supplemental (diffraction) measurements, where notable efforts have been reported for the former [48–51] and latter [52,53] approaches with more developments being underway.

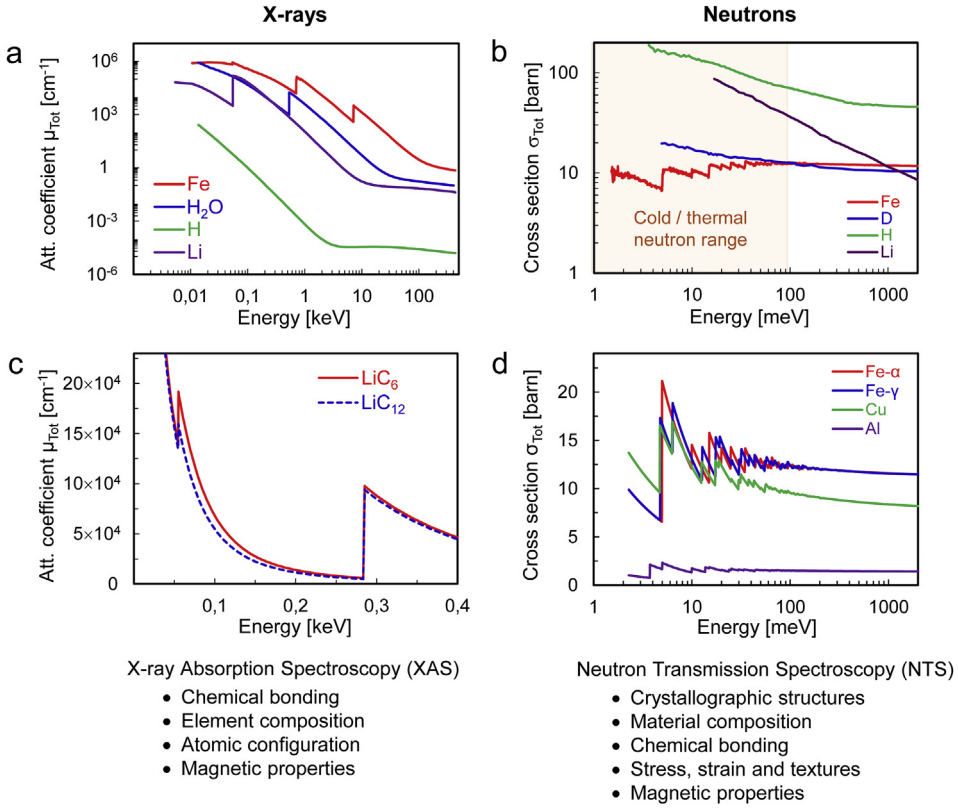

Fig. 1. Comparison between X-ray and neutron absorption imaging. (a) X-ray attenuation coefficients for some selected materials at different X-ray energies, (b) neutron cross sections for some selected mono-element phases at different neutron energies, (c) X-ray absorption edges of LiC_6 and LiC_{12} that are relevant in the context of electrode materials in batteries, and (d) neutron Bragg edges (cross sections per unit cell) for various metal structures.

The samples that we used herein to demonstrate the workflow and potential of spectral neutron tomography are polycrystalline and possess only a mild degree of texture even after plastic deformation. By reconstructing 3D volumes recorded at many different wavelengths (energies), we obtained a 4D data set, which allows us to display the wavelength-dependent attenuation coefficient in every voxel. In particular, we demonstrate that this spectral attenuation signal can be evaluated in every voxel within the sample volume to enable a much improved and more robust quantification of phase fractions than previously possible.

2. Experimental procedure

2.1. Collection of spectral tomographic data

The baseline for spectral neutron tomography is the collection of radiographic projections of a sample from different angles using different neutron wavelengths. The subsequent tomographic reconstruction of a sample volume is performed for individual wavelengths. One ends up with several sets of 3D sample volumes, each one containing the value of the attenuation coefficient for a single wavelength (more precisely for a narrow wavelength range depending on the resolution). In this way, every voxel of the sample contains a wavelength dependent attenuation spectrum, which can be used for further analysis e.g. for reducing the 4D information to a 3D volume representation of a certain wavelength dependent parameter such as the slope of the attenuation coefficient, the Bragg-edge position, height, or width.

For the example results presented herein, we collected data by using two different approaches for neutron wavelength (energy) selection: a double-crystal monochromatization (DCM) at a continuous neutron source and the TOF method at a pulsed neutron source. The former was performed at the neutron imaging beamline CONRAD-II at Helmholtz Zentrum Berlin [54,55] and the latter at the engineering beamline ENGIN-X at Rutherford Appleton Laboratory [20]. For the DCM setup, we recorded 200 angular radiographic projections distributed equally over 360 degrees at a single wavelength before selecting the next wavelength and then repeated the same procedure. In this fashion, we collected 20 tomographic data sets in a wavelength interval between 3.64 Å and 4.59 Å (20 bins in steps of 0.05 Å) within a total time of ~35 h (single exposure times of 30 s and a pixel size of 120 μm). By using the TOF approach and suitable detector technology providing a pixel size of 55 μm [56], we recorded data for the wavelength interval between 1.34 Å and 4.42 Å (≈2000 bins in steps of 0.00142 Å) at every radiographic projection. Using an exposure time of 1 h/projection (to obtain satisfactory counting statistics), we recorded 29 angular projections over 360 degrees using the golden ratio distribution [57] within ~30 h. Details about the experimental setups are described in the supplementary section.

2.2. Material and samples

Two sets of samples were prepared from the widely used alloy 304L (AISI), a low-carbon stainless steel with metastable austenite that exhibits the TRIP effect under plastic deformation. On mechanical loading, TRIP steels first undergo conventional dislocation plasticity. With larger deformation, the retained austenite progressively transforms into martensite, thereby increasing the work hardening rate at higher strain levels. This process gives rise to favorable properties such as high toughness and strength, and good corrosion resistance [58].

The martensitic phase transformation in steel has been repeatedly studied using the Bragg edge methodology. This is due to the strong diffraction power and clearly distinguishable characteristic Bragg edges [33,34,46,59–62]. Steels that may possess both of these phases are common, including metastable stainless steels that have outstanding formability (such as grade 304L), supermartensitic stainless steel that is widely used whenever welding is an issue [63] as well as the latest third-generation AHSS (advanced high-strength steels), to name a few. Table 1 shows the chemical composition of the material used.

Two sample geometries were manufactured and plastically deformed in torsion under well-controlled conditions using a custom built mechanical loading system [64]. A circular cross section of d = 8 mm (with a gauge length of 5 mm) was deformed to an angular twist of 179 degrees, corresponding to a maximum shear strain of 250%. The circular geometry allows one to apply high levels of plastic strain while the sample cross section is experiencing a strain distribution that increases radially from the center towards the outer diameter. While this presents a fairly simple case, the other sample with a rectangular cross section of 5 mm × 10 mm (gauge length = 7 mm), twisted to 464 degrees, experiences a much more complex strain distribution: Within the elastic regime, the maximum shear stresses in a rectangular cross section under pure torsion will occur at the midpoint of each longer side as analytically described in Refs. [65,66] but can be expected to deviate significantly once the geometry starts to evolve from its original dimensions due to the large plastic deformation. While numerical modelling can predict the strain distributions quite accurately as long as the geometrical boundary conditions are known, the predictions are challenged once the conditions start to change. The availability of full-field experimental characterization methods, such as spectral neutron tomography, is hence essential.

3. Results and discussion

3.1. Visualization and initial analysis of a 4D data set

The resulting 4D nature of the spectral neutron tomographic technique is shown in Fig. 2 for the rectangular TRIP steel sample (twisted to 464 degrees): Each reconstructed 3D volume contains the attenuation coefficients for a distinct neutron wavelength color-coded in cm^{-1}. Having recorded and reconstructed such images for a range of wavelengths, one can plot the wavelength dependent attenuation spectra for single 3D elements, either individual voxels or several voxels, termed volume of interest (VOI).

One can see in Fig. 2b that the attenuation value shows strong local variations up to a certain wavelength, after which the sample appears homogenous. This is due to the fact that no more Bragg scattering occurs beyond a certain wavelength for each phase (referred to as Bragg cut-off). The positions of the individual Bragg edges are described by Bragg's law $2d_{hkl}.\sin\theta = \lambda$, where 2θ corresponds to 180 degrees, λ is the wavelength and d_{hkl} is the atomic lattice spacing. As the sample is composed of both austenite and martensite, two distinct attenuation spectra are expected within the sample volume. The theoretical attenuation coefficients for the two phases were calculated using the software 'nxs plotter' [67] and are shown in Fig. 2c, while Fig. 2d shows two experimentally derived attenuation coefficient spectra. These correspond to two different VOIs, each with a voxel binning of 3 × 3 × 3 to improve the signal-to-noise ratio. The locations of the two VOIs are also shown Fig. 2b as well as in the horizontal cross sections through the sample shown in Fig. 2e.

From the curves shown in Fig. 2c, in combination with radiographic wavelength scans for a wider wavelength range between 2 Å and 4.5 Å, it can be concluded that the material represented by VOI#1 is purely austenitic (within the resolution limit). This region is located outside the gauge section of the torsion sample.

Table 1
Chemical compositions (wt.%) of the stainless steel 304L used in this study.

C	Co	Cr	Cu	Mn	Si	Mo	N	Ni	P	S	Fe
0.022	0.03	18.18	0.14	1.54	0.29	0.11	0.076	8.55	0.026	0.0017	Balance

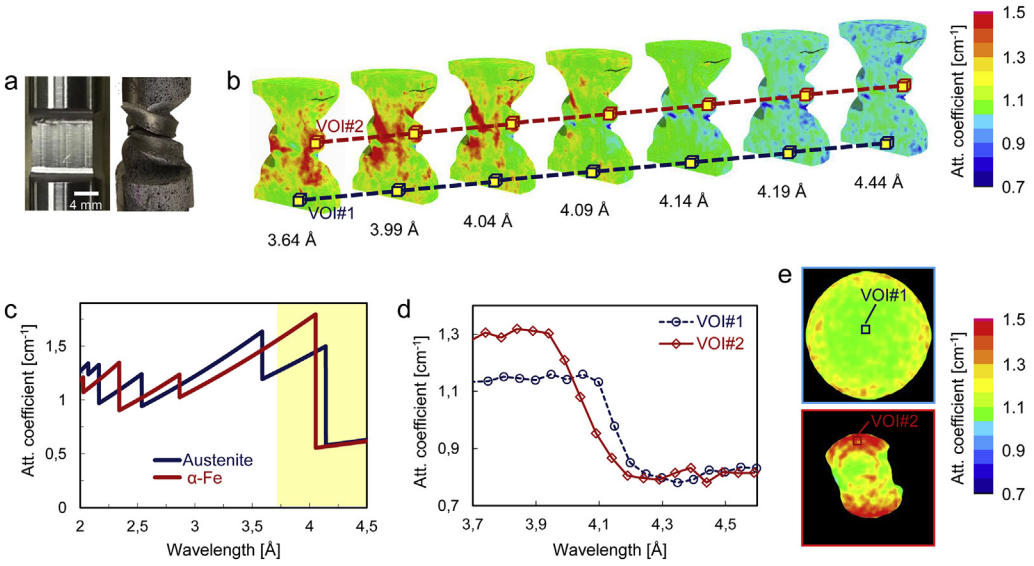

Fig. 2. The principle of spectral neutron tomography is depicted and based on a 4D data set. (a) Photograph of the undeformed sample with a rectangular cross section and of the measured torsion sample that was twisted to 464 degrees, (b) 3D rendering of the sample for data taken at different wavelengths with the attenuation coefficients represented by a color scheme, (c) theoretical attenuation coefficients for the two phases, where martensite has the same crystallographic structure as α-iron, (d) experimentally determined attenuation coefficients for the measured wavelength band for two separate volumes of interest (VOIs), (e) horizontal cross sections of the 3D volume at 3.64 Å highlighting the two VOIs shown in (d). Note: For graphs (c) and (d), neutron wavelengths are given unlike Fig. 1 where neutron energies are specified.

For the other location, VOI#2, a region inside the gauge section was selected that experienced large amounts of plastic deformation. One can observe that the position of the visible Bragg edge is notably different from that in VOI#1. The attenuation coefficient after the Bragg cut-off is the same, while a higher value is observed for wavelengths before these Bragg edges. Comparing these observations with the simulated data one can conclude that a martensitic phase transformation has taken place in this region. The simulated data further show that the two phases have Bragg edges around 4 Å at distinctively different positions, with the martensitic Bragg edge corresponding to bcc (110) and the austenitic Bragg edge corresponding to fcc (111). They are, however, in such proximity to each other that they are convoluted by the instrumental wavelength resolution when both present, hence rendering it impossible to quantify the phase fractions from one measurement alone. If the Bragg edge positions for the pure phases are known, regions in which these two phases simultaneously exist can be interpolated by analyzing the effective position of the observed Bragg edge.

The attenuation coefficients derived experimentally can be expected to still deviate from the calculated values due to instrumental effects and forward scattering of the sample. Both effects can to some extent be corrected [68–71] but are not crucial for the evaluation of the samples investigated herein in which these effects do not change between the samples and sample regions that are being compared.

3.2. Deriving wavelength-dependent attenuation parameters from a 4D data set (4D to 3D)

Since it is cumbersome and inconvenient to visualize 4D data volumes, the logical next data analysis step involves assigning a single value to each voxel of the 3D sample volume that is derived from the spectral information within. For the two samples that were investigated, we applied a fitting procedure on a voxel by voxel basis to determine the Bragg edge position. We applied the following mathematical algorithm: first, the derivative of the attenuation profiles (see Fig. 3a and b) was taken and second, this derivative was fitted by a Gaussian function:

$$f(\lambda) = f_0 + \frac{A}{w\sqrt{\pi/2}} e^{-2\frac{(\lambda-\lambda_c)^2}{w^2}}, \quad (1)$$

where $f(\lambda)$ is the Gaussian fitting function, f_0 an offset term, λ_c the peak position (hence the Bragg edge position), w describes the full width at half maximum (FWHM) and A is the height of the peak (A>0).

Fig. 3a and b show this procedure for two selected VOIs inside each sample. It is now possible to assign to each voxel a value for the Bragg edge position that can be represented by a color code as done in Fig. 3c and d for the rectangular and circular samples, respectively. Since the Bragg edge positions for the pure phases are known, one can now obtain a clearer picture of the localized phase transformation. For both samples, it is evident that no phase change has taken place in regions outside the gauge length as expected.

For the sample with the rectangular cross section, the prediction of the expected shears stress and phase distribution by analytical or numerical tools is challenging due to the large plastic deformation. The experimental results show that the regions closest to the shorter sides of the cross section have undergone the largest amount of phase transformation as well as that two opposing corners of the cross section show a much larger degree of phase transformation than the other two corners. This particular observation can be partly explained by geometrical constraints implied

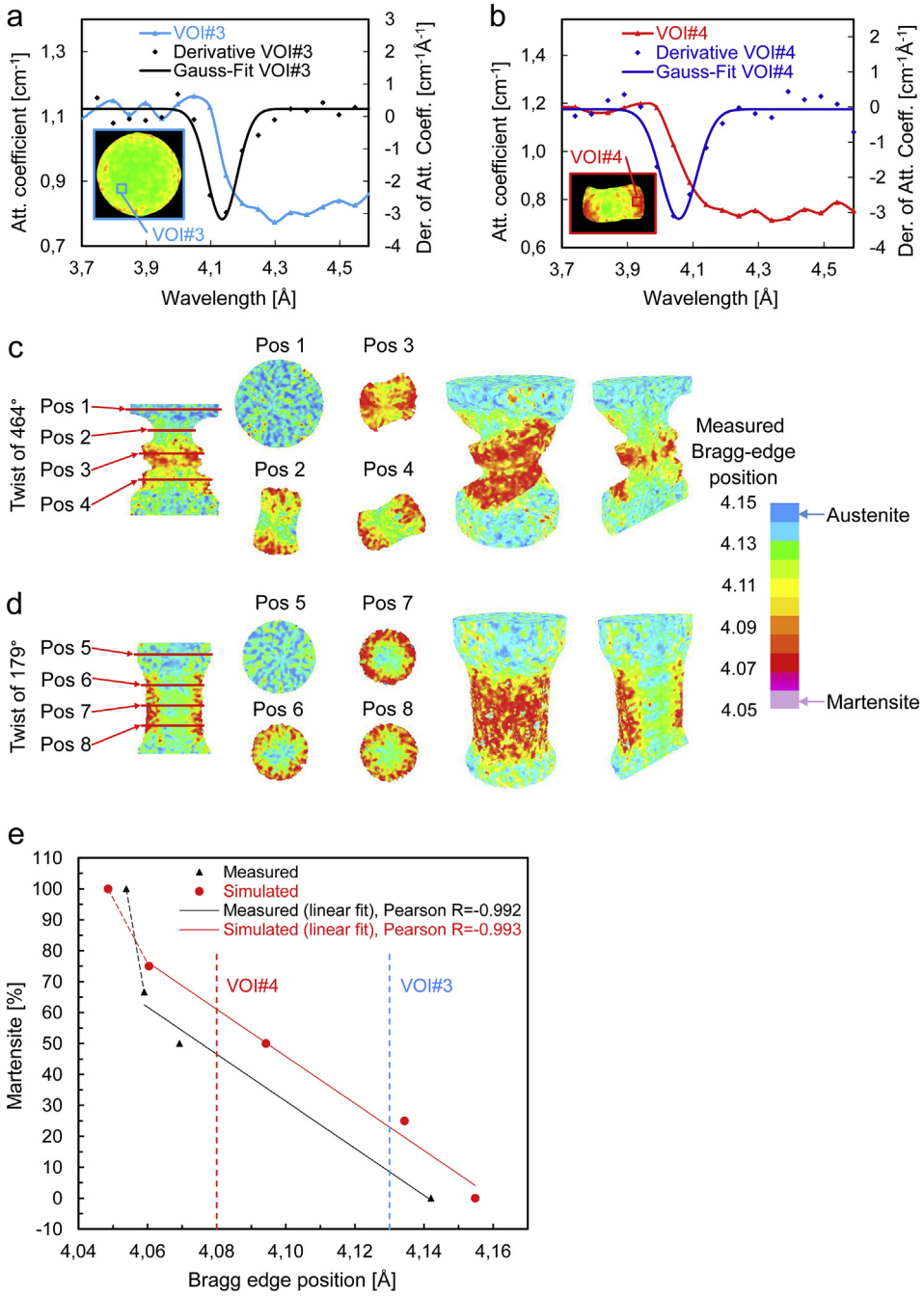

Fig. 3. (a) Profile of attenuation coefficients at the investigated Bragg edge, its derivative and a Gaussian fit for an example volume (VOI#3) that is located outside the gauge section, (b) same for another example volume (VOI#4) that is located towards the bottom of the gauge length of the rectangular cross section, (c) vertical and horizontal cross-sections as well as 3D representations for the rectangular sample showing the Bragg edge positions after 3D fitting, (d) and for the circular sample showing Bragg edge positions after 3D fitting, (e) Martensite phase fractions vs. Bragg edge positions as measured for the four calibration samples (black) and simulations for 100%, 75%, 50%, 25%, 0% martensite, where Bragg edge positions were determined using data in Fig. 2c (red). Vertical lines refer to data in a) and b).

by the gauge length and are actually supported by finite element modeling of the shear stress distributions, which will be discussed in detail in a separate publication.

The circular sample geometry yields results that are easier to interpret since the phase transformation progressed as expected and resulted in a radial distribution, moreover agreeing with previously reported results [32,33,72]. The 3D rendering of the well-characterized sample [32,33] actually allows to visualize that the effectively measured Bragg edge position changes incrementally with the radially progressing phase transformation.

3.3. Quantification of phase fractions using a calibration curve

The next step in determining phase fractions within a sample involves deriving a calibration curve that relates the measured Bragg edge with a certain phase fraction. The native parameter to associate with a phase fraction would be—in analogy to the height

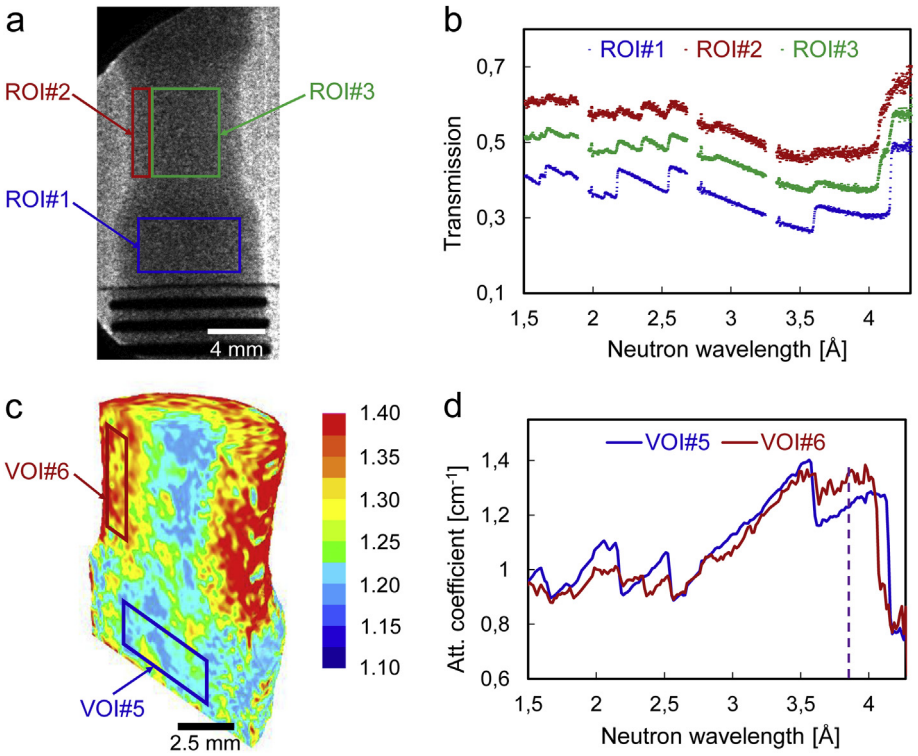

Fig. 4. Time-of-flight (TOF) transmission and attenuation coefficient profiles of the sample twisted by 179°. (a) Visualization of samples with region of interest (ROI) depicted that was used for the plot in (b), (b) Bragg-edge transmission spectra after normalizing (TOF radiographic projections between 2.0 Å and 4.4 Å with an exposure time of 3600 s/projection) for the different gauge areas of the sample, (c) 3D rendering of the sample at 3.85 Å based on TOF attenuation coefficients, highlighting the two VOI's displayed in the plot, (d) Attenuation coefficient profiles for the two selected VOI's in (c).

of Bragg peaks in diffraction measurements—the height of the Bragg edge(s). However, since the current measurements focused on Bragg edges for two phases that appear in close proximity, these can hardly be discerned, especially when convoluted with the instrumental resolution.

We hence propose another approach that allows to calibrate the effectively measured Bragg edge positions using known phase fractions. For this purpose, we performed calibration measurements using combinations of calibration samples with plate geometries of single-phase steel alloys, namely an austenitic stainless steel (fcc structure) and a ferritic steel (bcc structure), both with lattice parameters that are close to the ones expected from the phases in the samples under investigation (note that both, the ferritic steel and the formed martensite possess a bcc lattice structure). Neutron wavelength scans were performed between 2 Å and 5 Å in steps of 0.02 Å for these standard samples in the following combination: 1.0 cm austenitic steel; 0.5 cm austenitic steel +0.5 cm ferritic steel; 0.33 cm austenitic steel +0.67 cm ferritic steel and 1.0 cm ferritic steel. The fitting algorithm from Eq. (1) was applied to derive the Bragg edge positions for each pure and combined sample. The corresponding positions are shown as black triangles in Fig. 3e. The figure also contains simulated data points (red circles) for five different martensite fractions that were obtained using the theoretical attenuation spectra for similar combinations of austenitic and ferritic steel from nxs plotter [67] (compare Fig. 2c), which were convoluted by the instrumental resolution function. From the resulting curves the positions of the Bragg-edges were determined, see red points in Fig. 3e.

The derived calibration curves from both experimentally and simulated data points are non-linear as expected. We have attempted several different fits to the data points, but given that the relevant phase bcc fraction can be expected ≤75%, we have chosen a simple linear fit that describes the relationship between Bragg edge position and phase fraction well enough within the resolution limit of the measurements. The fitted lines to describe the phase fractions are as follows:

$$\text{Martensite,\%(simulated)} = 3168 - 761 \times (\text{Bragg edge position, Å})$$

$$\text{Martensite,\%(measured)} = 3149 - 760 \times (\text{Bragg edge position, Å})$$

Obviously, the two lines have almost the same slopes but are shifted by an offset in vertical direction. The reason for this is very likely the difference in composition of the investigated alloys and the simulated one, as that can result in different lattice parameters. Residual strain is not expected to have a significant impact on this difference (neither for the calibration samples nor for the twisted samples). It should be noted that the twisted samples have yet another alloying composition and another small systematic offset might be present as well. Nevertheless, a qualitative comparison and quantitative estimation could be made for the two VOIs given in Fig. 3a and b where the martensitic phase fraction is found to be approximately 10–20% for VOI#3 and 50–60% for VOI#4. This correlates well with the expected trend for more pronounced phase transition in areas of higher stresses observed in Fig. 3c and discussed above. The estimated phase fractions for VOI#3 and VOI#4 are in good agreement with previously reported results from neutron tomography, the Olson–Cohen model, neutron diffraction, and EBSD [73].

3.4. Spectral neutron tomography by time-of-flight

As it was shown above, spectral neutron tomography can be effectively implemented using a tunable monochromator at a

steady-state neutron source. The advantages include that well-established detector technology can be used that offers good detection efficiency, high spatial resolution, and large fields of view. The disadvantages include the limitation to thermal and cold neutrons (relatively low energies), the inefficiency associated with wavelength scanning and the relatively low wavelength resolution. These disadvantages can be overcome by implementing the method at spallation neutron sources combined with TOF techniques [20,22,35,74]. To provide a direct comparison between the two approaches we herein also include results that were obtained for one of the samples investigated at CONRAD-II, namely the one with the circular geometry, at the pulsed neutron instrument ENGIN-X [20].

Fig. 4 shows the neutron transmission spectra obtained for one radiographic projection (top) and the reconstructed 3D volume for which the attenuation spectrum can be plotted on a voxel level (4D data set, bottom). The highlighted region of interest #1 (ROI#1 in Fig. 4a) corresponds to an area outside the gauge section that remained fully austenitic. This can be readily confirmed by the transmission spectrum from a single radiographic projection as seen in Fig. 4b. The other two regions for which spectra are included, ROI#2 and ROI#3, both show additional Bragg edges indicating that austenite and martensite are present within the radiographic projection of that region. The spectra all differ in terms of absolute transmission values due the different material thickness of the selected regions. Compared to the data obtained by the DCM approach, one can already see from Fig. 4b that the two different Bragg edges around 4 Å, namely bcc (110) and fcc (111), are now clearly separated. It can furthermore be seen that the martensitic phase fraction is larger for ROI#2 than for ROI#3, which makes sense since the latter contains the center of the sample in addition to the outer radius section.

As explained in the methods section, tomographic reconstructions were performed for 200 wavelength bins, based on the same 29 individual radiographic projections. Fig. 4c shows the 3D rendering of the reconstructed volume at a wavelength of 3.85 Å where the two phases show clearly different attenuation coefficients. Attenuation coefficient spectra are presented in Fig. 4d for two VOIs that correspond to the ROIs depicted above. Each VOI is only one voxel deep in the other (not-indicated) dimension. One can immediately see that the interpretation of spectral imaging data becomes much easier with this approach, as the comparison with the predicted values in terms of attenuation coefficients removes the complexity of varying sample thicknesses. Not surprisingly, the VOI#5 closely resembles the predicted attenuation spectrum for austenite in Fig. 2c. Similar to ROI#2, the signal that is plotted for VOI#6 shows Bragg edges from both phases, and it is worth noting that the instrumental resolution allows us to separate the two individual Bragg edges around 4 Å, both before and after the tomographic reconstruction. The higher information content based on the larger wavelength bandwidth compared to the DCM data is apparent; however, in the present case it comes at the expense of fewer radiographic projections. The new imaging instruments at high-flux pulsed neutron sources in combination with efficient detector technology, possibly even based on fast CMOS cameras [75], are expected to lead to further improvements and faster measurement times.

4. Summary/conclusions

We reported on the use of spectral neutron tomography (an alternative terminology could be 'tomographic 4D neutron spectroscopy') and used it to obtain 3D data for phase fractions of austenite and martensite in samples made from TRIP steel. We demonstrated how the spectral signal can be evaluated on a voxel by voxel basis for the quantification of the two phase fractions. Samples with circular and rectangular cross sections have been subjected to high levels of plastic deformation, resulting in a localized phase transformation at regions experiencing high magnitudes of strain. For the circular cross section, we performed an analytical fitting of a 4D data set and combined it with a novel calibration approach, which confirmed previously reported results for the same sample, while the current method allows to identify potential texture biases more readily. The rectangular cross section presents a more challenging geometry resulting in a much more complex strain distribution, especially after severe plastic deformation, for which we were able to reveal the localized phase transformation across the complete volume non-destructively that is otherwise not accessible by any other method. The data presented herein were measured both at a steady-state neutron source using a double-crystal monochromator as well as at a spallation neutron source using the TOF technique.

By performing spectral neutron tomography, it is possible not only to display the wavelength dependent attenuation coefficients at a voxel level but also to evaluate this data in a quantitative manner that can be considered more robust and reliable than earlier approaches e.g. simple dual-energy tomography. It is important to note that the spectral tomography method is not limited to the analysis of crystalline materials and Bragg edges but can be expected to have major benefits for elemental discrimination across many disciplines, in analogy to the corresponding X-ray and electron based techniques [3,9,76]. We expect that the method benefits from implementation at both pulsed and steady-state sources with the latter being naturally suited to the analysis strategy described herein.

Data availability

The raw data required to reproduce the findings of this study are available from the corresponding author on reasonable request.

CRediT author statement

Khanh Van Tran: Methodology, Software, Investigation, Formal analysis, Writing – original draft, Visualization. **Robin Woracek:** Conceptualization, Methodology, Investigation, Formal analysis, Writing – original draft, Writing – review & editing, Visualization, Resources, Supervision. **Nikolay Kardjilov:** Conceptualization, Methodology, Software, Investigation, Formal analysis, Writing – original draft, Writing – review & editing, Visualization, Resources, Supervision. **Henning Markötter:** Software, Investigation, Writing – review & editing, Visualization. **André Hilger:** Software, Visualization, Resources, Formal analysis. **Winfried Kockelmann:** Investigation, Writing – review & editing. **Joe Kelleher:** Investigation, Resources. **Stephen Puplampu:** Investigation. **Dayakar Penumadu:** Funding acquisition, Resources, Supervision. **Anton S. Tremsin:** Resources, Investigation. **John Banhart:** Resources, Writing – review & editing, Supervision. **Ingo Manke:** Funding acquisition, Resources, Writing – review & editing, Supervision, Methodology, Formal analysis.

Declaration of competing interest

The authors declare that they have no known competing financial interests or personal relationships that could have appeared to influence the work reported in this article.

Acknowledgment

Funding: This work was supported by the Ministry of Education and Training of the Socialist Republic of Vietnam with project number 911 for overseas doctoral training.

Appendix A. Supplementary data

Supplementary data to this article can be found online at https://doi.org/10.1016/j.mtadv.2021.100132.

References

[1] C.H. McCollough, S. Leng, L. Yu, J.G. Fletcher, Dual-and multi-energy CT: principles, technical approaches, and clinical applications, Radiology 276 (2015) 637–653.
[2] E. Maire, P.J. Withers, Quantitative X-ray tomography, Int. Mater. Rev. 59 (2014) 1–43.
[3] C.K. Egan, S.D.M. Jacques, M.D. Wilson, M.C. Veale, P. Seller, A.M. Beale, R.A.D. Pattrick, P.J. Withers, R.J. Cernik, 3D chemical imaging in the laboratory by hyperspectral X-ray computed tomography, Sci. Rep. 5 (2015) 15979.
[4] S. Huotari, T. Pylkkänen, R. Verbeni, G. Monaco, K. Hämäläinen, Direct tomography with chemical-bond contrast, Nat. Mater. 10 (2011) 489–493.
[5] C.G. Schroer, M. Kuhlmann, T.F. Günzler, B. Lengeler, M. Richwin, B. Griesebock, D. Lützenkirchen-Hecht, R. Frahm, E. Ziegler, A. Mashayekhi, D.R. Haeffner, J.D. Grunwaldt, A. Baiker, Mapping the chemical states of an element inside a sample using tomographic x-ray absorption spectroscopy, Appl. Phys. Lett. 82 (2003) 3360–3362.
[6] T. Arlt, I. Manke, K. Wippermann, H. Riesemeier, J. Mergel, J. Banhart, Investigation of the local catalyst distribution in an aged direct methanol fuel cell MEA by means of differential synchrotron X-ray absorption edge imaging with high energy resolution, J. Power Sources 221 (2013) 210–216.
[7] M. Busi, K.A. Mohan, A.A. Dooraghi, K.M. Champley, H.E. Martz, U.L. Olsen, Method for system-independent material characterization from spectral X-ray CT, NDT E Int. 107 (2019) 102136.
[8] D. Jumanazarov, J. Koo, M. Busi, H.F. Poulsen, U.L. Olsen, M. Iovea, System-independent material classification through X-ray attenuation decomposition from spectral X-ray CT, NDT E Int. 116 (2020) 102336.
[9] G. Möbus, R.C. Doole, B.J. Inkson, Spectroscopic electron tomography, Ultramicroscopy 96 (2003) 433–451.
[10] P.A. Midgley, R.E. Dunin-Borkowski, Electron tomography and holography in materials science, Nat. Mater. 8 (2009) 271–280.
[11] G.N. Hounsfield, Computerized transverse axial scanning (tomography): Part 1. Description of system, Br. J. Radiol. 46 (1973) 1016–1022.
[12] R.E. Alvarez, A. MacOvski, Energy-selective reconstructions in X-ray computerised tomography, Phys. Med. Biol. 21 (1976) 733–744.
[13] N. Kardjilov, I. Manke, R. Woracek, A. Hilger, J. Banhart, Advances in neutron imaging, Mater. Today 21 (2018) 652–672.
[14] M. Strobl, I. Manke, N. Kardjilov, A. Hilger, M. Dawson, J. Banhart, Advances in neutron radiography and tomography, J. Phys. D Appl. Phys. 42 (2009).
[15] E.H. Lehmann, G. Frei, P. Vontobel, L. Josic, N. Kardjilov, A. Hilger, W. Kockelmann, A. Steuwer, The energy-selective option in neutron imaging, Nucl. Instruments Methods Phys. Res. Sect. A Accel. Spectrometers, Detect. Assoc. Equip. 603 (2009) 429–438.
[16] M. Strobl, B. Betz, R.P. Harti, A. Hilger, N. Kardjilov, I. Manke, C. Gruenzweig, Wavelength-dispersive dark-field contrast: micrometre structure resolution in neutron imaging with gratings, J. Appl. Crystallogr. 49 (2016) 569–573.
[17] R. Woracek, D. Penumadu, N. Kardjilov, A. Hilger, M. Strobl, R.C. Wimpory, I. Manke, J. Banhart, Neutron Bragg-edge-imaging for strain mapping under in situ tensile loading, J. Appl. Phys. 109 (2011) 1–5.
[18] W. Treimer, M. Strobl, N. Kardjilov, A. Hilger, I. Manke, Wavelength tunable device for neutron radiography and tomography, Appl. Phys. Lett. 89 (2006) 2004–2007.
[19] A.M. Al-Falahat, N. Kardjilov, T.V. Khanh, H. Markötter, M. Boin, R. Woracek, F. Salvemini, F. Grazzi, A. Hilger, S.S. Alrwashdeh, J. Banhart, I. Manke, Energy-selective neutron imaging by exploiting wavelength gradients of double crystal monochromators—simulations and experiments, Nucl. Instruments Methods Phys. Res. Sect. A Accel. Spectrometers, Detect. Assoc. Equip. 943 (2019) 162477.
[20] W. Kockelmann, G. Frei, E.H. Lehmann, P. Vontobel, J.R. Santisteban, Energy-selective neutron transmission imaging at a pulsed source, Nucl. Instruments Methods Phys. Res. Sect. A Accel. Spectrometers, Detect. Assoc. Equip. 578 (2007) 421–434.
[21] M. Strobl, N. Kardjilov, A. Hilger, D. Penumadu, I. Manke, Advanced neutron imaging methods with a potential to benefit from pulsed sources, Nucl. Instruments Methods Phys. Res. Sect. A Accel. Spectrometers, Detect. Assoc. Equip. 651 (2011) 57–61.
[22] R.O. Nelson, S.C. Vogel, J.F. Hunter, E.B. Watkins, A.S. Losko, A.S. Tremsin, N.P. Borges, T.E. Cutler, L.T. Dickman, M.A. Espy, Neutron imaging at LANSCE—from cold to ultrafast, J. Imaging. 4 (2018) 45.
[23] M. Strobl, R. Harti, C. Grünzweig, R. Woracek, J. Plomp, Small angle scattering in neutron imaging—a review, J. Imaging. 3 (2017) 64.
[24] M. Strobl, H. Heimonen, S. Schmidt, M. Sales, N. Kardjilov, A. Hilger, I. Manke, T. Shinohara, J. Valsecchi, Polarization measurements in neutron imaging, J. Phys. D Appl. Phys. 52 (2019) 123001.
[25] A. Hilger, I. Manke, N. Kardjilov, M. Osenberg, H. Markötter, J. Banhart, Tensorial neutron tomography of three-dimensional magnetic vector fields in bulk materials, Nat. Commun. 9 (2018).
[26] V.V. Zerkin, B. Pritychenko, The experimental nuclear reaction data (EXFOR): extended computer database and Web retrieval system, Nucl. Instruments Methods Phys. Res. Sect. A Accel. Spectrometers, Detect. Assoc. Equip. 888 (2018) 31–43.
[27] N. Soppera, M. Bossant, E. Dupont, Janis 4: an improved version of the NEA Java-based nuclear data information system, Nucl. Data Sheets 120 (2014) 294–296.
[28] R. Woracek, J. Santisteban, A. Fedrigo, M. Strobl, Diffraction in neutron imaging—a review, Nucl. Instruments Methods Phys. Res. Sect. A Accel. Spectrometers, Detect. Assoc. Equip. 878 (2018) 141–158.
[29] H. Sato, T. Kamiyama, Y. Kiyanagi, Pulsed neutron imaging using resonance transmission spectroscopy, Nucl. Instruments Methods Phys. Res. Sect. A Accel. Spectrometers, Detect. Assoc. Equip. 605 (2009) 36–39.
[30] A.S. Tremsin, J.B. McPhate, J. V Vallerga, O.H.W. Siegmund, W. Kockelmann, E.M. Schooneveld, N.J. Rhodes, W.B. Feller, High resolution neutron resonance absorption imaging at a pulsed neutron beamline, IEEE Trans. Nucl. Sci. 59 (2012) 3272–3277.
[31] M. Siegwart, R. Woracek, J.I. Márquez Damián, A.S. Tremsin, V. Manzi-Orezzoli, M. Strobl, T.J. Schmidt, P. Boillat, Distinction between super-cooled water and ice with high duty cycle time-of-flight neutron imaging, Rev. Sci. Instrum. 90 (2019).
[32] R. Woracek, D. Penumadu, N. Kardjilov, A. Hilger, M. Boin, J. Banhart, I. Manke, 3D mapping of crystallographic phase distribution using energy-selective neutron tomography, Adv. Mater. 26 (2014) 4069–4073.
[33] R. Woracek, D. Penumadu, N. Kardjilov, A. Hilger, M. Boin, J. Banhart, I. Manke, Neutron Bragg edge tomography for phase mapping, in: Phys. Procedia, Elsevier B.V., 2015, pp. 227–236.
[34] K. Watanabe, T. Minniti, H. Sato, A.S. Tremsin, W. Kockelmann, R. Dalgliesh, Y. Kiyanagi, Cross-sectional imaging of quenched region in a steel rod using energy-resolved neutron tomography, Nucl. Instruments Methods Phys. Res. Sect. A Accel. Spectrometers, Detect. Assoc. Equip. 944 (2019) 162532.
[35] C. Carminati, M. Strobl, T. Minniti, P. Boillat, J. Hovind, M. Morgano, T. Holm Rod, E. Polatidis, J. Valsecchi, D. Mannes, W. Kockelmann, A. Kaestner, Bragg-edge attenuation spectra at voxel level from 4D wavelength-resolved neutron tomography 4D wavelength-resolved neutron tomography, J. Appl. Crystallogr. 53 (2020) 188–196.
[36] C.M. Wensrich, J.N. Hendriks, A. Gregg, M.H. Meylan, V. Luzin, A.S. Tremsin, Bragg-edge neutron transmission strain tomography for in situ loadings, Nucl. Instrum. Methods Phys. Res. Sect. B Beam Interact. Mater. Atoms 383 (2016) 52–58.
[37] J.N. Hendriks, A.W.T. Gregg, C.M. Wensrich, A.S. Tremsin, T. Shinohara, M. Meylan, E.H. Kisi, V. Luzin, O. Kirsten, Bragg-edge elastic strain tomography for in situ systems from energy-resolved neutron transmission imaging, Phys. Rev. Mater. 1 (2017).
[38] J.N. Hendriks, C. Jidling, T.B. Schön, A. Wills, C.M. Wensrich, E.H. Kisi, Neutron transmission strain tomography for non-constant stress-free lattice spacing, Nucl. Instrum. Methods Phys. Res. Sect. B Beam Interact. Mater. Atoms 456 (2019) 64–73.
[39] H.J. Kirkwood, C.M. Wensrich, A.M. Paradowska, B. Abbey, Application and validity of the Radon transform applied to axisymmetric neutron strain imaging, Int. J. Solid Struct. 180–181 (2019) 137–146.
[40] G. Festa, E.P. Cippo, D. Di Martino, R. Cattaneo, R. Senesi, C. Andreani, E. Schooneveld, W. Kockelmann, N. Rhodes, A. Scherillo, Neutron resonance transmission imaging for 3D elemental mapping at the ISIS spallation neutron source, J. Anal. At. Spectrom. 30 (2015) 745–750.
[41] T. Kamiyama, J. Ito, H. Noda, H. Iwasa, Y. Kiyanagi, S. Ikeda, Computer tomography thermometry—an application of neutron resonance absorption spectroscopy, Nucl. Instruments Methods Phys. Res. Sect. A Accel. Spectrometers, Detect. Assoc. Equip. 542 (2005) 258–263.
[42] S.V. Venkatakrishnan, L. Dessieux, P. Bingham, Wavelength-resolved neutron tomography for crystalline materials, ICASSP, IEEE Int. Conf. Acoust. Speech Signal Process. - Proc. (2019-May) 7700–7704, 2019.
[43] A. Cereser, M. Strobl, S.A. Hall, A. Steuwer, R. Kiyanagi, A.S. Tremsin, E.B. Knudsen, T. Shinohara, P.K. Willendrup, A.B. da Silva Fanta, Time-of-flight three dimensional neutron diffraction in transmission mode for mapping crystal grain structures, Sci. Rep. 7 (2017) 1–11.
[44] S. Peetermans, A. King, W. Ludwig, P. Reischig, E.H. Lehmann, Cold neutron diffraction contrast tomography of polycrystalline material, Analyst 139 (2014) 5765–5771.
[45] M. Raventós, M. Tovar, M. Medarde, T. Shang, M. Strobl, S. Samothrakitis, E. Pomjakushina, C. Grünzweig, S. Schmidt, Laue three dimensional neutron diffraction, Sci. Rep. 9 (2019) 1–13.
[46] A. Steuwer, J.R. Santisteban, P.J. Withers, L. Edwards, Pattern decomposition and quantitative-phase analysis in pulsed neutron transmission, Phys. B Condens. Matter 350 (2004) 159–161.
[47] S. Vogel, P.D.H.-G. Priesmeyer, A Rietveld-Approach for the Analysis of Neutron Time-Of-Flight Transmission Data, Christian-Albrechts Universität zu

Kiel, 2000. http://eldiss.uni-kiel.de/macau/receive/dissertation_diss_00000330.
[48] F. Malamud, J.R. Santisteban, Full-pattern analysis of time-of-flight neutron transmission of mosaic crystals, J. Appl. Crystallogr. 49 (2016) 348–365.
[49] Q. Xie, G. Song, S. Gorti, A.D. Stoica, B. Radhakrishnan, J.C. Bilheux, M. Kirka, R. Dehoff, H.Z. Bilheux, K. An, Applying neutron transmission physics and 3D statistical full-field model to understand 2D Bragg-edge imaging, J. Appl. Phys. 123 (2018).
[50] L.L. Dessieux, A.D. Stoica, P.R. Bingham, Single crystal to polycrystal neutron transmission simulation, Rev. Sci. Instrum. 89 (2018) 25103.
[51] L.L. Dessieux, A.D. Stoica, P.R. Bingham, K. An, M.J. Frost, H.Z. Bilheux, Neutron transmission simulation of texture in polycrystalline materials, Nucl. Instrum. Methods Phys. Res. Sect. B Beam Interact. Mater. Atoms 459 (2019) 166–178.
[52] R. Woracek, J.R. Bunn, D. Penumadu, A. Tremsin, A. Siriruk, N. Kardjilov, I. Manke, M. Boin, A. Hilger, C.R. Hubbard, B. Clausen, T.A. Sisneros, Methodology for combined neutron diffraction and Bragg edge imaging, Mater. Res. Soc. Symp. Proc. 1528 (2013).
[53] M.J. Gutmann, W. Kockelmann, L.C. Chapon, P.G. Radaelli, Phase imaging using time-of-flight neutron diffraction, J. Appl. Crystallogr. 39 (2006) 82–89.
[54] Nikolay Kardjilov, André Hilger, Ingo Manke, Robin Woracek, John Banhart, CONRAD-2: the new neutron imaging instrument at the Helmholtz-Zentrum Berlin, J. Appl. Crystallogr. 49 (2016) 195–202.
[55] N. Kardjilov, A. Hilger, I. Manke, CONRAD-2: cold neutron tomography and radiography at BER II (V7), J. Large-Scale Res. Facil. JLSRF. 2 (2016).
[56] A.S. Tremsin, J.V. Vallerga, J.B. McPhate, O.H.W. Siegmund, Optimization of high count rate event counting detector with Microchannel Plates and quad Timepix readout, Nucl. Instruments Methods Phys. Res. Sect. A Accel. Spectrometers, Detect. Assoc. Equip. 787 (2015) 20–25.
[57] S. Wundrak, J. Paul, J. Ulrici, E. Hell, V. Rasche, A small surrogate for the golden angle in time-resolved radial MRI based on generalized fibonacci sequences, IEEE Trans. Med. Imag. 34 (2015) 1262–1269.
[58] W.D. Callister, D.G. Rethwisch, Materials Science and Engineering: an Introduction, seventh ed., John wiley & sons, New York, 2007.
[59] M.A.M. Bourke, J.G. Maldonado, D. Masters, K. Meggers, H.G. Priesmeyer, Real time measurement by Bragg edge diffraction of the reverse ($\alpha' \rightarrow \gamma$) transformation in a deformed 304 stainless steel, Mater. Sci. Eng. A221 (1996) 1–10.
[60] J.R. Santisteban, L. Edwards, M.E. Fizpatrick, A. Steuwer, P.J. Withers, Engineering applications of Bragg-edge neutron transmission, Appl. Phys. Mater. Sci. Process 74 (2002).
[61] A. Steuwer, P.J. Withers, J.R. Santisteban, L. Edwards, Using pulsed neutron transmission for crystalline phase imaging and analysis, J. Appl. Phys. 97 (2005).
[62] J. Huang, S.C. Vogel, W.J. Poole, M. Militzer, P. Jacques, The study of low-temperature austenite decomposition in a Fe-C-Mn-Si steel using the neutron Bragg edge transmission technique, Acta Mater. 55 (2007) 2683–2693.
[63] Eitan Dabah, Beate Pfretzschner, Thomas Schaupp, Nikolay Kardjilov, Ingo Manke, Mirko Boin, Robin Woracek, Axel Griesche, Time-resolved Bragg-edge neutron radiography for observing martensitic phase transformation from austenitized super martensitic steel, J. Mater. Sci. 52 (2017) 3490–3496.
[64] R. Woracek, J.R. Bunn, D. Penumadu, C.R. Hubbard, Method to determine hkl strains and shear moduli under torsion using neutron diffraction, Appl. Phys. Lett. 100 (2012) 1–6.
[65] R.G.B. Warren, C. Young, Roark's Formulas for Stress and Strain, seventh ed., McGraw-Hill Companies, Inc, New York, 2001.
[66] Jan Franců, Petra Nováčková, Přemysl Janíček, Torsion OF A NON-circular bar, in: Eng. Mech, 2012, pp. 45–60.
[67] M. Boin, nxs: a program library for neutron cross section calculations, J. Appl. Crystallogr. 45 (2012) 603–607.
[68] P. Boillat, C. Carminati, F. Schmid, C. Grünzweig, J. Hovind, A. Kaestner, D. Mannes, M. Morgano, M. Siegwart, P. Trtik, P. Vontobel, E.H. Lehmann, Chasing quantitative biases in neutron imaging with scintillator-camera detectors: a practical method with black body grids, Opt. Express. 26 (2018) 15769.
[69] C. Carminati, P. Boillat, F. Schmid, P. Vontobel, J. Hovind, M. Morgano, M. Raventos, M. Siegwart, D. Mannes, C. Gruenzweig, P. Trtik, E. Lehmann, M. Strobl, A. Kaestner, Implementation and assessment of the black body bias correction in quantitative neutron imaging, PloS One 14 (2019) 1–24.
[70] M. Raventós, E.H. Lehmann, M. Boin, M. Morgano, J. Hovind, R. Harti, J. Valsecchi, A. Kaestner, C. Carminati, P. Boillat, P. Trtik, F. Schmid, M. Siegwart, D. Mannes, M. Strobl, C. Grünzweig, A Monte Carlo approach for scattering correction towards quantitative neutron imaging of polycrystals, J. Appl. Crystallogr. 51 (2018) 386–394.
[71] A.M. Al-Falahat, A. Kupsch, M.P. Hentschel, A. Lange, N. Kardjilov, H. Markötter, I. Manke, Correction approach of detector backlighting in radiography, Rev. Sci. Instrum. 90 (2019).
[72] E. Cakmak, Investigation of the Phase Transformation Kinetics and Texture Evolution in a TRIP Steel under Complex Loads, The University of Tennessee, Knoxville, 2014.
[73] R. Woracek, Energy Selective Neutron Imaging for the Characterization of Polycrystalline Materials, The University of Tennessee, Knoxville, 2015. https://trace.tennessee.edu/utk_graddiss/3375.
[74] M. Strobl, Future prospects of imaging at spallation neutron sources, Nucl. Instruments Methods Phys. Res. Sect. A Accel. Spectrometers, Detect. Assoc. Equip. 604 (2009) 646–652.
[75] R. Woracek, M. Krzyzagorski, H. Markötter, P.M. Kadletz, N. Kardjilov, I. Manke, A. Hilger, Spatially resolved time-of-flight neutron imaging using a scintillator CMOS-camera detector with kHz time resolution, Opt. Express. 27 (2019) 26218.
[76] Y.H. Lo, C.-T. Liao, J. Zhou, A. Rana, C.S. Bevis, G. Gui, B. Enders, K.M. Cannon, Y.-S. Yu, R. Celestre, Multimodal x-ray and electron microscopy of the Allende meteorite, Sci. Adv. 5 (2019), eaax3009.